Ab Initio Design of Low Band Gap 2D Tin Organohalide Perovskites.

Alberto Fraccarollo, Leonardo Marchese, and Maurizio Cossi*

Dipartimento di Scienze e Innovazione Tecnologica (DISIT), Università del Piemonte Orientale, via T. Michel 11, I-15121, Alessandria, Italy

E-mail: maurizio.cossi@uniupo.it

Abstract

Four layered hybrid perovskites, based on tin iodide sheets intercalated by divalent organic cations (ethylenediammonium, 2,2'-biaziridinium, 2,2'-biimidazolium, 4,4'-bipyridinium), have been modeled with ab initio techniques. The crystal structures have been optimized at the DFT level, thus not including thermal effects, finding and characterizing three minima for each cation: with respect to the analogues with monovalent cations, the structures are more distorted and mostly in a staggered arrangement. The interlayer distances are quite small for all the systems, due to the single layer of strongly charged cations between the inorganic sheets. The band profiles and the band gaps, computed with an additive approach including the effects of spin orbit coupling and post-DFT correlation corrections, show an unexpected and interesting feature: with two of the cations some nearly degenerate low energy levels appear at the bottom of the conduction band. As a consequence, these systems present unusually low band gaps (the minimum value being 1.34 eV) suggesting the possibility of light adsorption in the visible or near-IR regions. The existence of these low lying levels has been correlated to the charge and the aromatic nature of the organic ions, and a simple molecular descriptor, based on the LUMO energy of the isolated cations, is proposed to design other tin iodide perovskites with this characteristic.

Introduction

Hybrid perovskites, formed by metal halide networks neutralized by organic cations, have been intensely studied in the last years[1–11] due to their extremely good performances in optoelectronics and photovoltaics (PV).[9,12–15] The perovskite solar cell conversion efficiency has exceeded 22%,[16] and even better results are expected in the next future: the best strategy proposed to date to attain high efficiencies is to

mix methylammonium and formamidinium cations with lead iodide and bromide;[17] another promising approach is the combination of perovskite cells with wideband IR organic absorbers.[18] Furthermore, many hybrid perovskites based on lead and tin halides show strong photoluminescence emissions,[19,20] with important applications in the production of light emitting diodes (LED)[21–23] and in general for optoelectronics.[2,24–27]

The correlation between chemical composition, geometrical structure and electronic properties is fundamental to design new perovskites for PV and optoelectronic applications: there is an enormous interest in tuning the band gap, the exciton binding energy and the charge transport properties by changing the metal,[6–8] the halide[9–11] and specially the organic cation.[28–32]

The best PV results are provided by perovskites with 3D structure, which can be achieved only for small cations, namely methylammonium and formamidinium (except some examples of perovskites including Cs^+ or ethylammonium):[33–35] steric limitations prevent the use of larger organic counterparts. On the other hand, layered perovskites can accomodate in the interlayer space a much greater variety of cations: these systems can have either a true 2D structure, in which metal tetrahalides (MX_4^{2-}) form layers of corner-sharing octahedra intercalated by mono- or divalent organic ions,[36–40] or a mixed-dimension structure, sometimes referred to as quasi-2D.[22,41–45] In the latter case, slabs of various thickness of 3D perovskites (comprising the small cations mentioned above) are intercalated by larger ions, giving rise to Ruddledsen-Popper phases which are being widely studied also for improving the stability and the efficiency of PV devices.[46–48]

The understanding of hybrid perovskites has been greatly improved by high level theoretical calculations, which described the properties of 3D[49–59] and 2D[1,30,59–64] systems with a variety of approaches. Most calculations were based on Density Functional Theory (DFT), sometimes including semiempirical corrections for van der Waals interactions: a number of studies have pointed out the great importance of spin orbit coupling (SOC) effects,[1,49,61,64] and many authors have demonstrated that also post-DFT correlation energy has to be included to obtain reliable band gap estimates.[49,54,65–69]

We have recently modeled with ab initio techniques[70,71] some homologue series

of 2D perovskites based on $(PbI_4)^{2-}$, $(SnI_4)^{2-}$ and $(SnBr_4)^{2-}$ layers intercalated by a variety of monovalent cations, describing the correlation between structures, electronic band profiles and band gaps. In every series, the band gaps were found to depend on the organic cations mainly through the geometrical parameters (interlayer distance and distortion of the inorganic octahedra); substituting Pb with Sn caused a substantial reduction of the band gap, which increased again when iodide was substituted with bromide. In all the systems, however, the computed band gap remained well above 2 eV, too large to allow the absorption of visible light and thus a direct PV application.

In this paper we extend the analysis to 2D hybrid perovskites formed by $(SnI_4)^{2-}$ layers intercalated by divalent cations: tin iodide systems provided the lowest band gaps with monovalent cations, and we expected that when the positive charge is concentrated in a *single* layer of divalent cations between the halide sheets, the interlayer distance could be reduced, possibly lowering the band gap further. Indeed, the not numerous members of this family whose structure has been resolved confirm this expectation: for SnI_4 perovskites with organic dications the cystallographic interlayer distances vary from 9.5 to 10.3 Å;[72–74] in PbI_4 analogues the range of interlayer distances is $10.3 - 13.7$ Å.[75–77] Furthermore, Mao and coworkers recently reported on a SnI_4 2D perovskite with the doubly charged histammonium cation, exhibiting optical absorption in the visible region.[78]

Four organic ions were considered, namely ethylenediammonium (EDA), 2,2'-biaziridinium (AZI), 2,2'-biimidazolium (IMI), 4,4'-bipyridinium (PYR), illustrated in Figure 1. EDA and AZI are among the smallest organic dications of this kind, thus allowing very short interlayer distances, while IMI and PYR include aromatic rings whose effects on the material electronic properties are worth studying.

Figure 1.

Methods

The geometry optimizations were performed with CRYSTAL09[79,80] at the DFT level, using the PBESOL-D2[81] functional and including the dispersion energy contri-

butions through the semiempirical procedure proposed by Grimme with the so-called D2 set of parameters;[82] note that in this procedure the dispersion terms affect the optimized geometries and the stability energies, but they do not enter the calculation of electronic properties. Both atomic positions and cell parameters were optimized and the nature of the stationary points was verified by computing numerically the second derivatives and diagonalizing the Hessian matrix. Dunning's correlation consistent cc-pVDZ basis set[83] was used, along with small core Stuttgart-Köln effective core potentials for Sn, Br and I.[84,85]

Some calculations on isolated cations were performed with Gaussian09,[86] using either pure (PBE, BLYP) or hybrid (B3LYP) density functionals, and Dunning's aug-cc-pVTZ triple-ζ basis set supplemented by polarization and diffuse functions.[87]

Electronic band structures and band gaps were computed with QUANTUM ESPRESSO code, based on plane waves expansion of the electronic density, with the PBE functional; electronic bands were computed on a 32 k-point path defined in the primitive Brillouin zone (illustrated in the Supporting Information). To evaluate SOC effects, the calculation of band structures and band gaps were repeated with scalar relativistic (SR) and full relativistic (FR) potentials (in the following FR-DFT indicates a calculation including SOC): the energy cutoffs were 70 Ryd with SR and 45 Ryd with FR potentials, respectively; a cutoff of 280 Ryd was also used for charge density expansions in FR-DFT. The contribution of the various atomic orbitals to the electronic bands was estimated with the projected density of states (PDOS), obtained using the atomic basis set provided by QUANTUM ESPRESSO.

The correlation energy was included at the GW level with the same functional, expanding the polarizability on a basis set with 3 Ryd cutoff and 2000 basis vectors.

Since the available version of QUANTUM ESPRESSO allows for GW calculations on the Γ point and with SR potentials only, in the previous works we have adopted an additive scheme to compute the band gap (E_g) with both SOC and correlation effects:[70,71]

$$E_g = E_g^{SR-DFT} + \left[E_g^{FR-DFT} - E_g^{SR-DFT}\right] + \left[E_g^{SR-GW}(\Gamma) - E_g^{SR-DFT}(\Gamma)\right] \quad (1)$$

where E_g^{SR-DFT} and E_g^{FR-DFT} are the band gaps obtained with scalar and full relativistic potentials, respectively, on the complete 32 k-point path, while $E_g^{SR-GW}(\Gamma)$ and $E_g^{SR-DFT}(\Gamma)$ are computed with and without GW correlation, respectively, on Γ point; the notation in eq. 1 is somehow redundant to highlight the SOC and GW additive corrections to the SR-DFT value.

Eq. 1 has been validated in refs. 70,71 by reproducing the structure and the band gap of the 3D perovskites $(CH_3NH_3)PbI_3$ and $(CH_3NH_3)SnI_3$, for which accurate experimental measures are available;[6,54,65,88,89] in the same works some methodological issues have been discussed, including the effect of the density functional and of the k-point path.

Results and discussion

Geometry optimizations

In previous papers[70,71] the optimization procedure was validated by reproducing the structure of (MA)PbI_3 and (MA)SnI_3 tri-dimensional perovskites (MA standing for methylammonium ion), and comparing the optimized and experimental structures of layered perovskites intercalated with phenylethylammonium.

Also in this case we check the method by comparing the optimized geometries with some of the few crystal structures of SnI_4 perovskites with divalent cations which have been resolved experimentally. Among the systems considered here, only one structure of (IMI)SnI_4 has been described, as a monoclinic crystal in $C2/c$ group (at 293 K);[72] the already cited perovskite intercalated with histammonium was assigned a monoclinic lattice in $P2_1/n$ group (298 K).[78] Another structure of this family, with N-ethylammonium-piperidinium (AEPi) dication, was reported in ref. 74 as a monoclinic lattice in $P2_1/c$ group (273 K).

Then the geometries of (IMI)SnI_4 and (AEPi)SnI_4 were optimized in the same crystal groups as in the original references, and the resulting cell parameters are compared to the experimental data in Table S1 in the Supporting Information (SI).

The agreement between the computed and experimental structures is very good, confirming the reliability of the procedure; the geometrical parameters of the inorganic layers are further discussed below.

In our models, however, we decided to explore the potential energy surfaces in greater detail, looking for minimum energy structures that can be hidden by high symmetry constraints. Then a larger freedom was given to cell parameters and atomic positions, optimizing all the structures as triclinic lattices, with $P\bar{1}$ group for (EDA)SnI_4 and (IMI)SnI_4, and $P1$ group for (AZI)SnI_4 and (PYR)SnI_4. It is worth to remind that the present calculations do not include any thermal contributions, so they are intended to reproduce "zero Kelvin" crystals; moreover, as a general remark about QM geometry optimizations, it should be remenbered that they allow to explore only some portions of the potential energy surface.

The procedure used to look for the potential energy minima is detailed in the SI: eventually three structures were optimized for all the systems, starting from three different guesses. The optimized structures are designated in the following as **x**-A (shorthand for **x**-(A)SnI_4), where $\mathrm{A} = \mathrm{EDA}, \mathrm{AZI}, \mathrm{IMI}, \mathrm{PYR}$ indicates the cation and $\mathbf{x} = \mathbf{1}, \mathbf{2}, \mathbf{3}$ specifies the initial system from which the minimization started (see the SI for more information). All the stationary points were confirmed to be true minima by diagonalizing the Hessian matrix: the eigenvalues resulted all positive except for **3**-IMI, where one negative value was obtained, so that this system was re-optimized with symmetry lowered to $P1$, until a true minimum was found.

The relative stability of the different structures was evaluated by computing at the same level the energy of the reaction:

$$\mathrm{SnI_{2(s)}} + 2\mathrm{I^-} + \mathrm{A^{2+}} \longrightarrow (\mathrm{A})\mathrm{SnI_{4(s)}} \tag{2}$$

where (s) indicates periodic solids, while ions are considered isolated species; SnI_2(s) structure (resolved at 273 K) was taken from ref. 90. Clearly, eq. 2 is not intended to reproduce the actual perovskites formation reaction, but only to provide a common energy scale; note that the "formation energies" from eq. 2 are not corrected for the BSSE (basis set superposition error), due to the presence of periodic systems with charged fragments.

All the optimized perovskites are depicted in Figure 2, and the corresponding Crystal Information Files (CIF) are provided in the SI; the cell parameters, the unit cell densities and the relative energies are reported in Table 1. Another view of the optimized structures, along the [001] direction, is also shown in the SI (Figure S2).

Figure 2.
Table 1.

The very similar density and energy data for **2**- and **3**-PYR suggest that the optimizations could have led to the same structure, though the definition of the cell parameters differs, as discussed below. For all the systems, the trend of the cell density with the structures is **1** < **2** < **3**, corresponding to closer packings of the successive layers (see below). Due to the nature essentially electrostatic of the interlayer interactions, the more closely packed structures also have lower energies: in all the cases, **3**-(A)SnI_4 systems are the most stable.

Layer stacking

It is well known that inorganic layered perovskites crystallize either in eclipsed or in staggered arrangements, depending on the stacking of metal atoms in adjacent layers (viewed normal to the layers),[91,92] and the same classification is often used for hybrid organic-inorganic perovskites too.[37,93] In this case it has been observed that mono/divalent cations tend to favor the staggered/eclipsed conformation, respectively,[93] and that eclipsed structures are facilitated in general by bulkier or longer chain cations;[36,39] several phase transitions have been described, noting that at higher temperatures the eclipsed arrangement tends to be more stable.[36,39,40,94] Staggered structures are often resolved in the monoclinic system, while orthorhombic cells are typically found for eclipsed systems.[36,37,40]

The stacking in 2D perovskites can be appreciated visually by projecting the metal atoms from one layer onto the underlying layer: this is shown for our optimized structures in the SI (Figure S3). All **2** and **3** structures can be considered staggered, while **1** structures, which have been optimized starting from an eclipsed arrangement, appear almost eclipsed for the larger cations, i.e. IMI and PYR, while for EDA and AZI the upper layer positions are clearly displaced. Apparently, with

small divalent ions the interlayer interactions are optimized by packing the octahedra in a staggered arrangement, independently of the starting geometry: we recall once again, however, that these results do not include thermal effects.

Layer geometry

The geometry of the inorganic layers is described through the equatorial (l_{eq}) and polar (l_p) Sn − I distances, the interlayer distance (d) and three angles measuring the in-plane Sn-I-Sn deviation from linearity (β), the octahedra tilting with respect to the inorganic layers (θ), and the I-Sn-I bending inside the octahedra (ϕ). These quantities describe the distortion of the tin iodide layers with respect to an ideal arrangement of perfectly aligned octahedra, with the polar bonds perpendicular to the layer plane: some of them are illustrated in Figure 3(a-d), and their values are listed in Table 2 for all the optimized structures.

Figure 3.
Table 2.

Since these systems have a single layer of organic cations, their interlayer distances tend to be quite small, even with cations of large molecular size, compared to the analogues with monovalent ions:[71] for instance, in the structures with IMI and PYR the interlayer distances (8.85 − 11.33 Å) are much shorter than in $(PEA)_2SnI_4$ (14.6−17.5 Å in DFT optimizations[71] or 16.3 Å in crystallographic measurement[95]), where PEA = phenylethylammonium. On the other hand, the systems with small monovalent (formamidinium and methylimidazolium) and divalent (EDA and AZI) cations have similar d values, suggesting that 8 Å is about the minimum interlayer distance for 2D tin iodide perovskites (the data presented in refs. 70 and 71 hint that this observation holds for lead iodide and tin bromide, too).

The in-plane metal displacement is in general smaller than in the monovalent ion analogues, with the exception of **2**- and **3**-EDA, as well as the octahedra deformation (measured by angle ϕ); the octahedra tilting (angle θ), on the other hand, is large and similar for all the systems, in the range $30 - 40^{\circ}$. This feature is likely due to the small interlayer distances of all the systems, which generate quite crowded interlayer spaces and induce the octahedra tilting.

Another measure of the deformation is the span of metal-iodide bond lengths, which is larger for **2**- and particularly for **3**- structures, i.e. the arrangements with shorter interlayer distances and closer packings.

As mentioned above, the reliability of the optimization method has been checked by reproducing the structure of two systems recently characterized, (IMI)SnI_4[72] and (AEPi)SnI_4:[74] in Table S2 (SI) the inorganic layer geometries are compared with the crystallographic data, finding an excellent agreement between the optimized and experimental parameters in $C2/c$ group. In addition, Table S2 also reports the parameters of **2**-IMI optimized as a triclinic lattice with $P\bar{1}$ group, to allow a direct comparison with the $C2/c$ crystallographic and theoretical structures: one can see that relasing the symmetry affects the layer structure only marginally, leaving the interlayer distance also unchanged. The main difference in the $P\bar{1}$ optimization is the shift of the layers with respect to each other, leading to a more staggered structure, as noted above; furthermore, the cell density increases from 3.19 to 3.53 g/cm^3 passing from $C2/c$ to $P\bar{1}$ group. This feature, as well as the higher symmetry of the experimental structure, can be ascribed to the thermal motions of the organic layer; it remains to explore to what extent this reflects on the electronic properties, as discussed in the following.

The possible formation of H-bonds between the protonated cations and the halide ions is considered an important feature in hybrid perovskites,[30,38] affecting the stability and the electronic properties: to evaluate the occurrence of H-bonding, the shortest NH$\cdots$I distance was selected for each optimized structure and the corresponding bond distances and angles are reported in the SI (Table S3). For most systems, a H-bond of medium strength is found on the basis of these geometrical parameters: the strongest interactions are seen in **1**-EDA, **3**-AZI, **2**- and **3**-IMI, whereas H-bonds seem almost negligible in all the (PYR)SnI_4 structures. Note however that temperature dependent molecular disorder in the organic layer can question the extent, or even the occurrence, of actual H-bonding in such systems: as pointed out above, DFT calculations do not provide information about the thermal effects, and describe better low temperature phases.

Finally, the geometrical parameters of **2**- and **3**-PYR are quite similar, but not coincident: this point, along with the very alike densities, formation energies and layer stacking seen above, suggest that the potential energy surface is quite flat.

Band structures and PDOS

The energy profiles along the selected k-point path, computed at FR-DFT level, are shown in Figure 4; the analogous SR-DFT results are reported in the SI (Figure S4).

Figure 4.

SR- and FR-DFT profiles are very similar to each other qualitatively, though the latter present systematically lower valence-conduction gaps as a consequence of SOC effects. Either direct or indirect band gaps are found for the various systems, without a clear trend: all the gaps are listed in the SI (Table S4). Note however that in many cases the top valence and/or the bottom conduction bands are quite flat, giving rise to several quasi-direct gaps: this is particularly evident in (IMI)SnI_4 and (PYR)SnI_4. For comparison, eclipsed/staggered SnI_4 perovskites with monovalent ions presented direct/indirect gaps, respectively,[71] while an opposite trend, with significant exceptions, was reported for lead iodide 2D perovskites with a number of different cations.[70]

The most remarkable feature in the band profiles emerge for all (IMI)SnI_4 and (PYR)SnI_4 structures, where a family of nearly degenerate levels appears at the bottom of the conduction band. These levels are almost independent of the k point, and especially for (PYR)SnI_4 they look like intra-gap states rather than actual conduction bands; the same feature is present both in SR- and in FR-DFT profiles.

The chemical nature of these energy levels can be clarified by projecting the electronic density on a set of localized gaussian-type atomic orbitals. The projected densities of states (PDOS) computed at FR-DFT level around the Fermi level are reported in Figure 5; the PDOS at the SR-DFT level are shown in the SI (Figure S5), along with the FR-DFT results computed in a wider energy range (Figure S6).

Figure 5.

It is clear that with IMI and PYR cations there is a large contribution of the organic layer to the low-energy empty levels, which is completely absent with EDA and AZI. In fact, in the former case the bottom conduction band is largely dominated by nitrogen and carbon orbitals, with a very limited contribution from iodine atoms;

on the other hand, the top valence band is always due to inorganic layer atoms, as already found for tin and lead 2D perovskites with monovalent cations. From Figures S5 and S6 in the SI, it is clear that the same features are obtained with both SR and FR potentials. This aspect is visually confirmed by the isodensity surface plot of the lowest unoccupied level in **3**-IMI, reported in the SI (Figure S7), computed with Gaussian09 and periodic boundary conditions (PBC) with PBE functional and the same basis set and effective core potentials used in the geometry optimizations described above. The electronic density appears strongly confined in the interlayer space, with onyl small contributions of the polar iodide ions, embedded in the organic layer.

To our knowledge, this feature was reported previously once,[96] for $PbBr_4$ layered perovskite intercalated by N-(3-aminopropyl)imidazolium dication: in this system, the DFT calculations revealed a low lying conduction band formed principally by nitrogen and carbon p orbitals, around 1 eV above the valence band composed mainly by bromide orbitals.

Band gaps

All the computed band gaps, split into the various contributions described in Section "Methods", are listed in Table 3.

Table 3.

The SR-DFT values reflect the trend illustrated by the band profiles in Figure 4: E_g^{SR} is much smaller in **1**- and **3**- (IMI)SnI_4 and (PYR)SnI_4 than in the other systems; **2**-IMI gap is slightly larger, close to the value of **2**-EDA, which in turn is smaller than in **1**- and **3**-EDA. On the other hand, all the values reported in Table 3 for **2**- and **3**-PYR are very similar, confirming that they can be considered as one system.

At the FR-DFT level the band gaps are systematically smaller than with SR potentials, meaning a negative SOC correction, while GW corrections (computed in Γ point as explained in Section "Methods") are always positive. As already observed for lead and tin halide perovskites with monovalent ions, SOC and GW effects do not

compensate and the latter prevails in all the cases, so that our best estimated band gaps (E_g) are always larger than the SR-DFT values. These results confirm that both SOC and GW effects are needed to obtain reliable gap estimates, as already noted for other 3D and 2D hybrid perovskites.[54,61,69,97,98]

SOC corrections are very similar for all the systems (ranging from -0.22 to -0.29 eV), with the exception of **3**-EDA and **3**-IMI, where they are quite smaller: apparently, SOC is not affected by the presence of the low lying levels due to the organic layer in (IMI)SnI_4 and (PYR)SnI_4. The size of SOC effects is similar to that computed at the same level for tin halide perovskites with monovalent cations in staggered arrangement, while the effect for eclipsed structures was somehow smaller.[71] A recent paper[69] reviewed several studies in which SOC corrections for lead and tin perovskites, both 3D and layered, were correlated to the structural parameters.[65,99,100] As discussed above, the structures optimized in this work show similar values for the octahedra tilting, while a larger variation is found for M-X-M angles: these changes, however, do not reflect on the computed SOC values. On the other hand, comparing the present results with those obtained at the same level for PbI_4 and SnI_4 HOP,[70,71] we find the expected trends with atomic energy levels, with increasing corrections when the atomic number grows from Sn to Pb, and from Br to I, in agreement with the analysis presented in ref. 59.

The values of the GW correction are much more scattered, the lowest being found in **2**-IMI (0.62 eV) and the highest in **1**-AZI (1.69 eV): also in this case, no clear correlation appears between the GW correction size and the presence of the low lying levels. We remind that in the present procedure GW calculations are limited to Γ point: possibly, the dispersion of GW values could be reduced if a more accurate k-space sampling were available, and this is a point which deserves to be considered in future work.

The most relevant results are listed in the last column of Table 3, reporting the best estimates of the band gap, including SOC and GW corrections. The E_g's for (EDA)SnI_4 and (AZI)SnI_4 are in line with the values previously computed for SnI_4 perovskites with monovalent cations (considering their small interlayer distances). In contrast, **2**-IMI, **2**-PYR and **3**-IMI present unusually low band gaps, well below the values measured or predicted so far for 2D hybrid perovskites: the lowest value (1.34 eV) is computed for **3**-IMI, but also for the other systems the estimated gap

falls in the visible spectral region.

As shown in Table 3, the minimum value for **3**-IMI derives mainly from the very small gap computed at the SR-DFT level (actually, the lowest among the studied systems) and a quite small GW correction, which is not the smallest one, however. The influence of SOC is clearly less important: besides varying little among all the systems, the least favorable SOC correction (-0.13 eV only) is computed for **3**-IMI, i.e. the perovskite with the smallest estimated gap. In general, it appears that all the small band gaps are related to the presence of the low lying electronic levels concentrated in the organic layer, and that low SR-DFT values lead to low E_g's too.

Clearly, such small band gaps are very interesting for optoelectronic and photovoltaic applications: if these results could be confirmed by experimental measures, it would be possible to produce 2D hybrid perovskites absorbing in the visible, or even in the near-IR regions. Due to the nature of the low lying levels discussed above, the excited electrons could be localized in the organic layers, possibly giving rise to hole conduction, though electron conduction cannot be excluded either, for iodide ions also contribute to these levels.

As mentioned above, a 2D tin iodide perovskite with histammonium (HA) cations was found to absorb in the visible region, with a band gap estimated from the Kubelka-Munk (KM) function of 1.67 eV:[78] in the same work, the band profiles were computed at the SR-DFT level and the band gap was estimated at 1.34 eV. We repeated the band gap calculation for this system using eq. 1 and keeping the crystal structure reported in ref. 78: E_g^{SR} resulted 1.02 eV, SOC and GW corrections -0.21 eV and 1.28 eV, respectively, and the final value was E_g = 2.08 eV. The difference in E_g^{SR} can be due to a higher energy cutoff and a denser mesh of k-points in the present calculation: in both cases, however, the band structure shows no low lying levels close to the Fermi level, and in our calculation the PDOS of the bottom conduction band does not contain significant contributions from the organic layer. In fact, the estimated E_g (2.08 eV) is similar to the values obtained for (EDA)SnI_4 and (AZI)SnI_4: the lower energy transition measured by the KM curve could be attributed to excitons, whose coupling energy has been estimated around 0.300 eV for this kind of systems.[2,63]

It is also interesting to evaluate the effect of the symmetry constraints imposed

during the geometry optimization, especially for the systems with the smallest band gaps. The electronic bands were computed for the $C2/c$ structure of **2**-IMI used for the comparison with the experimental crystal data: in the SI file (Figure S8) the band profile is compared to that of the same system optimized in $P\bar{1}$ group, clearly showing the strict similarity of the bands in the two cases. The agreement is confirmed by the calculation of the contributions to the band gap: in the $C2/c$ structure E_g^{SR} resulted 1.16 eV (1.19 eV in $P\bar{1}$, Table 3), SOC and GW corrections were -0.17 (-0.24) and 0.64 (0.62) eV, respectively, and the final estimate was 1.63 (1.57) eV. Increasing the symmetry, as in the crystallographic structure, has a limited effect on the gap values, and the interesting feature of such a small band gap is maintained also in $C2/c$ geometry.

The correlation between the inorganic layer structure and the band gaps computed at the semiempirical and DFT levels has been discussed recently[1,99] for homologue series of PbI_4 and SnI_4 hybrid perovskites. As shown in Table 2, the geometrical parameters with the largest effect on the band gap were found to be the in-plane M-X-M angle and the octahedra tilting (angles β, Figure 3-a, and θ, Figure 3-b); a strong dependence of the band gap on the M-X-M angle was predicted also in 3D (MA)PbI_3 by DFT calculations.[101] Among the systems studied here, such an analysis is sensible only with EDA and AZI cations, since in the other perovskites the band gaps are strongly influenced by the organic layers, as discussed above. In all the optimized structures with EDA and AZI we find very similar values for θ, quite larger than the angles reported in ref. 1 for lead iodide perovskites with monovalent ions: apparently, the intercalated dications pull the inorganic layers so close to distorce the octahedra orientation strongly and to a similar extent for all the systems. Angles β, as well as the interlayer distances d, vary more significantly in the various structures: comparing the data in Tables 2 and 3 we see that E_g^{SR} and E_g^{FR} follow parallel trends but a scarse correlation can be found with β and d. On the other hand, the best estimates of E_g, including GW contributions too, follow clearer trends: with EDA E_g decreases as β and d decrease, and with AZI a good linear correlation exists between E_g and d. The present data, however, are too limited to draw clear conclusions: this point will deserve a further analysis.

A molecular descriptor

The unexpected and intriguing electronic feature found for (IMI)SnI_4 and (PYR)SnI_4 is highly dependent on the nature of the organic layer: indeed, the low lying levels at the bottom conduction band are strongly localized and their PDOS show a predominant contribution from nitrogen and carbon atoms, unlike the other systems considered here. In order to design other 2D perovskites with the same characteristic, it would be very useful to relate the presence of these levels to the electronic structure of the isolated cations.

To verify this point, the geometry of the four cations under study was optimized with G09 using B3LYP density functional and aug-cc-pVTZ basis set; then the energy of the highest occupied and lowest unoccupied orbitals was computed with PBE functional and the same basis set. The same procedure was applied to histammonium, to check the results described above.

The results are illustrated in Figure 6: the energies of IMI and PYR lowest unoccupied molecular orbital (LUMO) are very similar, and lower than in the other cations. On this basis, the cation LUMO energy could be used as a test to predict whether a hybrid SnI_4 perovskite is likely to have low lying conduction bands localized in the organic layer: for instance, this property would correctly exclude such bands with HA.

Figure 6

Apparently, a cation needs a LUMO with particularly low energy to give rise to conduction bands near the Fermi level of tin iodide perovskites: IMI and PYR are divalent cations with both the nitrogen atoms involved in aromatic rings, two conditions expected to lower the energy of empty orbitals. On the other hand, EDA and AZI are non aromatic divalent cations, while in HA only one of the protonated nitrogen atoms belongs to an aromatic ring.

The orbital energies were obtained with PBE to keep close to the plane waves procedure: however, the same quantities have been computed also with BLYP and B3LYP functionals, with the results reported in the SI (Figures S9, S10). BLYP and PBE energies are very close to each other, while B3LYP provides a larger HOMO-LUMO gap, as expected with a hybrid functional, with higher energies for all the

empty orbitals: however, the same trend among the cations is reproduced by B3LYP also, as IMI and PYR LUMO energy is clearly lower than the others. From the data tabulated in the SI (Table S5), we conclude that cations with LUMO energy below -11 eV (computed with pure functionals, PBE or BLYP) or below -10.50 eV (with B3LYP) are likely candidates to produce low band gap SnI_4 perovskites.

Conclusions

We have optimized the structure and described the electronic properties of four 2D perovskites, formed by $(SnI_4)^{2-}$ layers intercalated by divalent organic cations. The procedure had been previously applied to analogue series of tin and lead halide perovskites with monovalent cations: in particular, the band gaps have been carefully estimated with scalar relativistic potentials on a suitable k-point path, and then corrected for SOC and GW effects through an additive scheme already applied and verified.

For all the perovskites, the exploration of the potential energy surfaces led to three minima (though in a case two minima were shown to correspond to one structure): with respect to the analogues with monovalent cations, these systems are more distorted and it is difficult to describe them as eclipsed or staggered, particularly with the smallest cations.

The analysis of the band profiles and band gaps led to an unexpected interesting feature: with two cations, 2,2'-biimidazolium (IMI) and 4,4'-bipyridinium (PYR), some nearly degenerate levels appeared at the bottom of the conduction band, almost independent of the k-point and largely dominated by the nitrogen and carbon orbitals. These levels are strongly localized in the interlayer space and they lead to unusually low band gaps: one of the optimized structures of (IMI)SnI_4 exhibits a band gap as low as 1.34 eV and other structures of (IMI)SnI_4 and (PYR)SnI_4 have values in the range 1.57-1.78 eV.

Such feature, reported previously only once for a hybrid perovskite, could allow the adsorption of near-IR or visible light: this point deserves further investigations, and we hope that the present results will prompt the synthesis and the experimental

characterization of this kind of materials.

To support the design of other tin iodide perovskites with the same characteristic, we propose a simple molecular descriptor, i.e. the LUMO energy of the isolated cations: the present models indicate that cations with LUMO energies lower than -11 eV (if computed with pure functionals) or -10.50 eV (with B3LYP) are likely candidates for this kind of perovskites.

Supporting Information

The Supporting Information is available free of charge on the ACS Publications website at DOI:

Coordinates of k-points; details about the crystal structure optimizations and layer stacking; FR-DFT band profiles; band gaps; PDOS; plot of the bottom conductiond band; cation LUMO energies (PDF).

Optimized crystal structures (CIF).

Acknowledgement

This work was funded by EU in the framework of the HORIZON2020 program, through the project MULTI2HYCAT (NMBP-01-2016-720783), and by the Italian Ministry of Education, University and Research (PRIN-2010A2FSS9).

References

(1) Pedesseau, L.; Sapori, D.; Traore, B.; Robles, R.; Fang, H.-H.; Loi, M.; Tsai, H.; Nie, W.; Blancon, J.-C.; Neukirch, A. et al. Advances and Promises of Layered Halide Hybrid Perovskite Semiconductors. *ACS Nano* **2016**, *10*, 9776–9786.

(2) Saparov, B.; Mitzi, D. Organic-Inorganic Perovskites: Structural Versatility for Functional Materials Design. *Chem. Rev.* **2016**, *116*, 4558–4596.

(3) Collavini, S.; Völker, S.; Delgado, J. Understanding the Outstanding Power Conversion Efficiency of Perovskite-Based Solar Cells. *Angew. Chem. Int. Ed.* **2015**, *54*, 9757–9759.

(4) Green, M.; Ho-Baillie, A.; Snaith, H. The Emergence of Perovskite Solar Cells. *Nat. Photonics* **2014**, *8*, 506–514.

(5) Park, N.-G. Organometal Perovskite Light Absorbers Toward a 20% Efficiency Low-cost Solid-state Mesoscopic Solar Cell. *J. Phys. Chem. Letters* **2013**, *4*, 2423–2429.

(6) Stoumpos, C. C.; Malliakas, C. D.; Kanatzidis, M. G. Semiconducting Tin and Lead Iodide Perovskites with Organic Cations: Phase Transitions, High Mobilities, and Near-Infrared Photoluminescent Properties. *Inorg. Chem.* **2013**, *52*, 9019–9038.

(7) Noel, N.; Stranks, S.; Abate, A.; Wehrenfennig, C.; Guarnera, S.; Haghighirad, A.-A.; Sadhanala, A.; Eperon, G.; Pathak, S.; Johnston, M. et al. Lead-free Organic-inorganic Tin Halide Perovskites for Photovoltaic Applications. *Energy Environ. Sci.* **2014**, *7*, 3061–3068.

(8) Hao, F.; Stoumpos, C.; Cao, D.; Chang, R.; Kanatzidis, M. Lead-free Solid-state Organic-inorganic Halide Perovskite Solar Cells. *Nat. Photonics* **2014**, *8*, 489–494.

(9) Lee, M.; Teuscher, J.; Miyasaka, T.; Murakami, T.; Snaith, H. Efficient Hybrid Solar Cells Based on Meso-superstructured Organometal Halide Perovskites. *Science* **2012**, *338*, 643–647.

(10) Liu, M.; Johnston, M.; Snaith, H. Efficient Planar Heterojunction Perovskite Solar Cells By Vapour Deposition. *Nature* **2013**, *501*, 395–398.

(11) Noh, J.; Im, S.; Heo, J.; Mandal, T.; Seok, S. Chemical Management for Colorful, Efficient, and Stable Inorganic-organic Hybrid Nanostructured Solar Cells. *Nano Lett.* **2013**, *13*, 1764–1769.

(12) Saliba, M.; Matsui, T.; Seo, J.-Y.; Domanski, K.; Correa-Baena, J.-P.; Nazeeruddin, M.; Zakeeruddin, S.; Tress, W.; Abate, A.; Hagfeldt, A. et al. Cesium-containing Triple Cation Perovskite Solar Cells: Improved Stability, Reproducibility and High Efficiency. *Energy Environ. Sci.* **2016**, *9*, 1989–1997.

(13) Bi, D.; Tress, W.; Dar, M.; Gao, P.; Luo, J.; Renevier, C.; Schenk, K.; Abate, A.; Giordano, F.; Correa Baena, J.-P. et al. Efficient Luminescent Solar Cells Based on Tailored Mixed-cation Perovskites. *Sci. Adv.* **2016**, *2*, e1501170.

(14) Zhou, H.; Chen, Q.; Li, G.; Luo, S.; Song, T.-B.; Duan, H.-S.; Hong, Z.; You, J.; Liu, Y.; Yang, Y. Interface Engineering of Highly Efficient Perovskite Solar Cells. *Science* **2014**, *345*, 542–546.

(15) Kim, H.-S.; Lee, C.-R.; Im, J.-H.; Lee, K.-B.; Moehl, T.; Marchioro, A.; Moon, S.-J.; Humphry-Baker, R.; Yum, J.-H.; Moser, J. E. et al. Lead Iodide Perovskite Sensitized All-Solid-State Submicron Thin Film Mesoscopic Solar Cell with Efficiency Exceeding 9%. *Sci. Rep.* **2012**, *2*, 591.

(16) Yang, W.; Park, B.-W.; Jung, E.; Jeon, N.; Kim, Y.; Lee, D.; Shin, S.; Seo, J.; Kim, E.; Noh, J. et al. Iodide Management in Formamidinium-lead-halide-based Perovskite Layers for Efficient Solar Cells. *Science* **2017**, *356*, 1376–1379.

(17) Seo, J.; Noh, J.; Seok, S. Rational Strategies for Efficient Perovskite Solar Cells. *Acc. Chem. Res.* **2016**, *49*, 562–572.

(18) Kinoshita, T.; Nonomura, K.; Jeon, N. J.; Giordano, F.; Abate, A.; Uchida, S.; Kubo, T.; Seok, S. I.; Nazeeruddin, M. K.; Hagfeldt, A. et al. Spectral Splitting

Photovoltaics Using Perovskite and Wideband Dye-sensitized Solar Cells. *Nat. Commun.* **2015**, *6*, 8834.

(19) Dohner, E.; Jaffe, A.; Bradshaw, L.; Karunadasa, H. Intrinsic White-light Emission from Layered Hybrid Perovskites. *J. Am. Chem. Soc.* **2014**, *136*, 13154–13157.

(20) Smith, M.; Jaffe, A.; Dohner, E.; Lindenberg, A.; Karunadasa, H. Structural Origins of Broadband Emission from Layered Pb-Br Hybrid Perovskites. *Chem. Sci.* **2017**, *8*, 4497–4504.

(21) Thirumal, K.; Chong, W.; Xie, W.; Ganguly, R.; Muduli, S.; Sherburne, M.; Asta, M.; Mhaisalkar, S.; Sum, T.; Soo, H. et al. Morphology-Independent Stable White-Light Emission from Self-Assembled Two-Dimensional Perovskites Driven By Strong Exciton-Phonon Coupling to the Organic Framework. *Chem. Mater.* **2017**, *29*, 3947–3953.

(22) Yuan, M.; Quan, L.; Comin, R.; Walters, G.; Sabatini, R.; Voznyy, O.; Hoogland, S.; Zhao, Y.; Beauregard, E.; Kanjanaboos, P. et al. Perovskite Energy Funnels for Efficient Light-emitting Diodes. *Nat. Nanotechnol.* **2016**, *11*, 872–877.

(23) Kim, Y.-H.; Cho, H.; Lee, T.-W. Metal Halide Perovskite Light Emitters. *Proc. Natl. Acad. Sci. U.S.A.* **2016**, *113*, 11694–11702.

(24) Chen, Q.; De Marco, N.; Yang, Y.; Song, T.-B.; Chen, C.-C.; Zhao, H.; Hong, Z.; Zhou, H.; Yang, Y. Under the Spotlight: the Organic-inorganic Hybrid Halide Perovskite for Optoelectronic Applications. *Nano Today* **2015**, *10*, 355–396.

(25) Tan, Z.-K.; Moghaddam, R.; Lai, M.; Docampo, P.; Higler, R.; Deschler, F.; Price, M.; Sadhanala, A.; Pazos, L.; Credgington, D. et al. Bright Light-emitting Diodes Based on Organometal Halide Perovskite. *Nat. Nanotech.* **2014**, *9*, 687–692.

(26) Deschler, F.; Price, M.; Pathak, S.; Klintberg, L.; Jarausch, D.-D.; Higler, R.; Httner, S.; Leijtens, T.; Stranks, S.; Snaith, H. et al. High Photoluminescence Effi-

ciency and Optically Pumped Lasing in Solution-processed Mixed Halide Perovskite Semiconductors. *J. Phys. Chem. Lett.* **2014**, *5*, 1421–1426.

(27) Smith, I.; Smith, M.; Jaffe, A.; Lin, Y.; Karunadasa, H. Between the Sheets: Post-synthetic Transformations in Hybrid Perovskites. *Chem. Mater.* **2017**, *29*, 1868–1884.

(28) Mitzi, D. A Layered Solution Crystal Growth Technique and the Crystal Structure of $(C_6H_5C_2H_4NH_3)_2PbCl_4$. *J. Solid State Chem.* **1999**, *145*, 694–704.

(29) Gauthron, K.; Lauret, J.-S.; Doyennette, L.; Lanty, G.; Choueiry, A.; Zhang, S.; Brehier, A.; Largeau, L.; Mauguin, O.; Bloch, J. et al. Optical Spectroscopy of Two-dimensional Layered $(C_6H_5C_2H_4NH_3)_2PbI_4$Perovskite. *Opt. Express* **2010**, *18*, 5912–5919.

(30) Sourisseau, S.; Louvain, N.; Bi, W.; Mercier, N.; Rondeau, D.; Boucher, F.; Buzaré, J.-Y.; Legein, C. Reduced Band Gap Hybrid Perovskites Resulting from Combined Hydrogen and Halogen Bonding At the Organic-inorganic Interface. *Chem. Mater.* **2007**, *19*, 600–607.

(31) Cao, D.; Stoumpos, C.; Farha, O.; Hupp, J.; Kanatzidis, M. 2D Homologous Perovskites as Light-Absorbing Materials for Solar Cell Applications. *J. Am. Chem. Soc.* **2015**, *137*, 7843–7850.

(32) Stoumpos, C.; Mao, L.; Malliakas, C.; Kanatzidis, M. Structure-Band Gap Relationships in Hexagonal Polytypes and Low-Dimensional Structures of Hybrid Tin Iodide Perovskites. *Inorg. Chem.* **2017**, *56*, 56–73.

(33) Yi, C.; Luo, J.; Meloni, S.; Boziki, A.; Ashari-Astani, N.; Grätzel, C.; Zakeeruddin, S.; Röthlisberger, U.; Grätzel, M. Entropic Stabilization of Mixed A-cation ABX3 Metal Halide Perovskites for High Performance Perovskite Solar Cells. *Energy Environ. Sci.* **2016**, *9*, 656–662.

(34) Im, J.-H.; Chung, J.; Kim, S.-J.; Park, N.-G. Synthesis, Structure, and Photovoltaic Property of a Nanocrystalline 2H Perovskite-type Novel Sensitizer $(CH_3CH_2NH_3)PbI_3$. *Nanoscale Res. Lett.* **2012**, *7*, 1–14.

(35) Peng, W.; Miao, X.; Adinolfi, V.; Alarousu, E.; El Tall, O.; Emwas, A.-H.; Zhao, C.; Walters, G.; Liu, J.; Ouellette, O. et al. Engineering of $CH_3NH_3PbI_3$ Perovskite Crystals By Alloying Large Organic Cations for Enhanced Thermal Stability and Transport Properties. *Angew. Chem. Int. Ed.* **2016**, *55*, 10686–10690.

(36) Lemmerer, A.; Billing, D. Synthesis, Characterization and Phase Transitions of the Inorganic-organic Layered Perovskite-type Hybrids $[(C_nH_{2n+1}NH_3)_2PbI_4]$, n = 7, 8, 9 and 10. *Dalton. Trans.* **2012**, *41*, 1146–1157.

(37) Lemmerer, A.; Billing, D. Effect of Heteroatoms in the Inorganic-organic Layered Perovskite-type Hybrids $[(ZC_nH_{2n}NH_3)2PbI_4]$, n = 2, 3, 4, 5, 6; Z = OH, Br and I; and $[(H_3NC_2H_4S_2C_2H_4NH_3)PbI_4]$. *CrystEngComm* **2010**, *12*, 1290–1301.

(38) Mitzi, D. In *Progress in Inorganic Chemistry*; Karlin, K., Ed.; John Wiley & Sons, Inc., 2007; pp 1–121.

(39) Billing, D.; Lemmerer, A. Synthesis, Characterization and Phase Transitions in the Inorganic-organic Layered Perovskite-type Hybrids $[(C_nH_{2n+1}NH_3)_2PbI_4]$, n = 4, 5 and 6. *Acta Crystallogr., Sect. B: Struct. Sci.* **2007**, *63*, 735–747.

(40) Billing, D.; Lemmerer, A. Inorganic-organic Hybrid Materials Incorporating Primary Cyclic Ammonium Cations: the Lead Iodide Series. *CrystEngComm* **2007**, *9*, 236–244.

(41) Jung, M.-H. Photovoltaic Effect of 2D Homologous Perovskites. *Electrochim. Acta* **2017**, *240*, 98–107.

(42) Gan, X.; Wang, O.; Liu, K.; Du, X.; Guo, L.; Liu, H. 2D Homologous Organic-inorganic Hybrids as Light-absorbers for Planer and Nanorod-based Perovskite Solar Cells. *Sol. Energy Mater. Sol. Cells* **2017**, *162*, 93–102.

(43) Vassilakopoulou, A.; Papadatos, D.; Koutselas, I. Light Emitting Diodes Based on Blends of Quasi-2D Lead Halide Perovskites Stabilized within Mesoporous Silica Matrix. *Micropor. Mesopor. Mat.* **2017**, *249*, 165–175.

(44) Quan, L.; Zhao, Y.; Garca De Arquer, F.; Sabatini, R.; Walters, G.; Voznyy, O.; Comin, R.; Li, Y.; Fan, J.; Tan, H. et al. Tailoring the Energy Landscape in Quasi-2D Halide Perovskites Enables Efficient Green-Light Emission. *Nano Lett.* **2017**, *17*, 3701–3709.

(45) Chen, Y.; Sun, Y.; Peng, J.; Zhang, W.; Su, X.; Zheng, K.; Pullerits, T.; Liang, Z. Tailoring Organic Cation of 2D Air-Stable Organometal Halide Perovskites for Highly Efficient Planar Solar Cells. *Adv. Energy Mater.* **2017**,

(46) Stoumpos, C.; Soe, C.; Tsai, H.; Nie, W.; Blancon, J.-C.; Cao, D.; Liu, F.; Traor, B.; Katan, C.; Even, J. et al. High Members of the 2D Ruddlesden-Popper Halide Perovskites: Synthesis, Optical Properties, and Solar Cells of $(CH_3(CH_2)_3NH_3)_2(CH_3NH_3)_4Pb_5I_{16}$. *Chem* **2017**, *2*, 427–440.

(47) Blancon, J.-C.; Tsai, H.; Nie, W.; Stoumpos, C.; Pedesseau, L.; Katan, C.; Kepenekian, M.; Soe, C.; Appavoo, K.; Sfeir, M. et al. Extremely Efficient Internal Exciton Dissociation Through Edge States in Layered 2D Perovskites. *Science* **2017**, *355*, 1288–1292.

(48) Tsai, H.; Nie, W.; Blancon, J.-C.; Stoumpos, C.; Asadpour, R.; Harutyunyan, B.; Neukirch, A.; Verduzco, R.; Crochet, J.; Tretiak, S. et al. High-efficiency Two-dimensional Ruddlesden-Popper Perovskite Solar Cells. *Nature* **2016**, *536*, 312–317.

(49) Even, J.; Pedesseau, L.; Jancu, J.-M.; Katan, C. Importance of Spin–Orbit Coupling in Hybrid Organic/Inorganic Perovskites for Photovoltaic Applications. *J. Phys. Chem. Lett.* **2013**, *4*, 2999–3005.

(50) Mosconi, E.; Amat, A.; Nazeeruddin, M. K.; Grätzel, M.; De Angelis, F. First-Principles Modeling of Mixed Halide Organometal Perovskites for Photovoltaic Applications. *J. Phys. Chem. C* **2013**, *117*, 13902–13913.

(51) Brivio, F.; Walker, A.; Walsh, A. Structural and Electronic Properties of Hybrid Perovskites for High-efficiency Thin-film Photovoltaics from First-principles. *APL Mater.* **2013**, *1*, 042111.

(52) Yin, W.-J.; Shi, T.; Yan, Y. Unique Properties of Halide Perovskites as Possible Origins of the Superior Solar Cell Performance. *Advanced Materials* **2014**, *26*, 4653–4658.

(53) Kim, J.; Lee, S.-H.; Lee, J.; Hong, K.-H. The Role of Intrinsic Defects in Methylammonium Lead Iodide Perovskite. *J. Phys. Chem. Lett.* **2014**, *5*, 1312–1317.

(54) Umari, P.; Mosconi, E.; De Angelis, F. Relativistic GW Calculations on $CH_3NH_3PbI_3$ and $CH_3NH_3SnI_3$ Perovskites for Solar Cell Applications. *Sci. Rep.* **2014**, *4*, 4467.

(55) Mosconi, E.; Ronca, E.; De Angelis, F. First-principles Investigation of the TiO_2/Organohalide Perovskites Interface: the Role of Interfacial Chlorine. *J. Phys. Chem. Lett.* **2014**, *5*, 2619–2625.

(56) Torres, A.; Rego, L. Surface Effects and Adsorption of Methoxy Anchors on Hybrid Lead Iodide Perovskites: Insights for Spiro-MeOTAD Attachment. *J. Phys. Chem. C* **2014**, *118*, 26947–26954.

(57) Mosconi, E.; Umari, P.; De Angelis, F. Electronic and Optical Properties of Mixed

Sn-Pb Organohalide Perovskites: a First Principles Investigation. *J. Mater. Chem. A* **2015**, *3*, 9208–9215.

(58) Zhang, L.; Sit, P.-L. Ab Initio Study of Interaction of Water, Hydroxyl Radicals, and Hydroxide Ions with $CH_3NH_3PbI_3$ and $CH_3NH_3PbBr_3$Surfaces. *J. Phys. Chem. C* **2015**, *119*, 22370–22378.

(59) Even, J.; Pedesseau, L.; Katan, C.; Kepenekian, M.; Lauret, J.-S.; Sapori, D.; Deleporte, E. Solid-state Physics Perspective on Hybrid Perovskite Semiconductors. *J. Phys. Chem. C* **2015**, *119*, 10161–10177.

(60) Umebayashi, T.; Asai, K.; Kondo, T.; Nakao, A. Electronic Structures of Lead Iodide Based Low-Dimensional Crystals. *Phys. Rev. B Condens. Matter Mater. Phys.* **2003**, *67*, 1554051–1554056.

(61) Even, J.; Pedesseau, L.; Dupertuis, M.-A.; Jancu, J.-M.; Katan, C. Electronic Model for Self-assembled Hybrid Organic/Perovskite Semiconductors: Reverse Band Edge Electronic States Ordering and Spin-orbit Coupling. *Phys. Rev. B Condens. Matter Mater. Phys.* **2012**, *86*, 205301.

(62) Wang, D.; Wen, B.; Zhu, Y.-N.; Tong, C.-J.; Tang, Z.-K.; Liu, L.-M. First-Principles Study of Novel Two-Dimensional $(C_4H_9NH_3)_2PbX_4$ Perovskites for Solar Cell Absorbers. *J. Phys. Chem. Lett.* **2017**, *8*, 876–883.

(63) Cortecchia, D.; Neutzner, S.; Kandada, A.; Mosconi, E.; Meggiolaro, D.; De Angelis, F.; Soci, C.; Petrozza, A. Broadband Emission in Two-dimensional Hybrid Perovskites: the Role of Structural Deformation. *J. Am. Chem. Soc.* **2017**, *139*, 39–42.

(64) Pedesseau, L.; Jancu, J.-M.; Rolland, A.; Deleporte, E.; Katan, C.; Even, J. Electronic Properties of 2D and 3D Hybrid Organic/Inorganic Perovskites for Optoelectronic and Photovoltaic Applications. *Opt. Quant. Electron.* **2014**, *46*, 1225–1232.

(65) Amat, A.; Mosconi, E.; Ronca, E.; Quarti, C.; Umari, P.; Nazeeruddin, M.; Grätzel, M.; De Angelis, F. Cation-induced Band-gap Tuning in Organohalide Perovskites: Interplay of Spin-orbit Coupling and Octahedra Tilting. *Nano Letters* **2014**, *14*, 3608–3616.

(66) Brivio, F.; Butler, K.; Walsh, A.; Van Schilfgaarde, M. Relativistic Quasiparticle Self-consistent Electronic Structure of Hybrid Halide Perovskite Photovoltaic Absorbers. *Phys. Rev. B Condens. Matter Mater. Phys.* **2014**, *89*, 155204.

(67) Even, J.; Pedesseau, L.; Jancu, J.-M.; Katan, C. DFT and K P Modelling of the Phase Transitions of Lead and Tin Halide Perovskites for Photovoltaic Cells. *Phys. Status Solidi RRL* **2014**, *8*, 31–35.

(68) Menéndez-Proupin, E.; Palacios, P.; Wahnón, P.; Conesa, J. C. Self-consistent Relativistic Band Structure of the $CH_3NH_3PbI_3$ Perovskite. *Phys. Rev. B* **2014**, *90*, 045207.

(69) Katan, C.; Pedesseau, L.; Kepenekian, M.; Rolland, A.; Even, J. Interplay of Spin-orbit Coupling and Lattice Distortion in Metal Substituted 3D Tri-chloride Hybrid Perovskites. *J. Mater. Chem. A* **2015**, *3*, 9232–9240.

(70) Fraccarollo, A.; Cantatore, V.; Boschetto, G.; Marchese, L.; Cossi, M. Ab Initio Modeling of 2D Layered Organohalide Lead Perovskites. *J. Chem. Phys.* **2016**, *144*, 164701.

(71) Fraccarollo, A.; Canti, L.; Marchese, L.; Cossi, M. First Principles Study of 2D Layered Organohalide Tin Perovskites. *J. Chem. Phys.* **2017**, *146*, 234703.

(72) Tang, Z.; Guan, J.; Guloy, A. Synthesis and Crystal Structure of New Organic-based Layered Perovskites with 2,2-biimidazolium Cations. *J. Mater. Chem.* **2001**, *11*, 479–482.

(73) Xu, Z.; Mitzi, D.; Medeiros, D. $[(CH_3)_3NCH_2CH_2NH_3]SnI_4$: a Layered Perovskite with Quaternary/primary Ammonium Dications and Short Interlayer Iodine-iodine Contacts. *Inorg. Chem.* **2003**, *42*, 1400–1402.

(74) Takahashi, Y.; Obara, R.; Nakagawa, K.; Nakano, M.; Tokita, J.-Y.; Inabe, T. Tunable Charge Transport in Soluble Organic-inorganic Hybrid Semiconductors. *Chem. Mater.* **2007**, *19*, 6312–6316.

(75) Safdari, M.; Svensson, P.; Hoang, M.; Oh, I.; Kloo, L.; Gardner, J. Layered 2D Alkyldiammonium Lead Iodide Perovskites: Synthesis, Characterization, and Use in Solar Cells. *J. Mater. Chem. A* **2016**, *4*, 15638–15646.

(76) Nageswara Rao, K.; Singh, A.; Vijaya Prakash, G. Synthesis, Structure and Optical Studies of Inorganic-organic Hybrid Semiconductor, $(H_3NC_6H_4CH_2NH_3PbI_4)$. *Materials Research Bulletin* **2014**, *52*, 78–81.

(77) Hautzinger, M. P.; Dai, J.; Ji, Y.; Fu, Y.; Chen, J.; Guzei, I. A.; Wright, J. C.; Li, Y.; Jin, S. Two-Dimensional Lead Halide Perovskites Templated By a Conjugated Asymmetric Diammonium. *Inorganic Chemistry* **2017**, *ASAP*, null.

(78) Mao, L.; Tsai, H.; Nie, W.; Ma, L.; Im, J.; Stoumpos, C.; Malliakas, C.; Hao, F.; Wasielewski, M.; Mohite, A. et al. Role of Organic Counterion in Lead- and Tin-Based Two-Dimensional Semiconducting Iodide Perovskites and Application in Planar Solar Cells. *Chem. Mater.* **2016**, *28*, 7781–7792.

(79) Dovesi, R.; Orlando, R.; Civalleri, B.; Roetti, C.; Saunders, V.; Zicovich-Wilson, C. CRYSTAL: a Computational Tool for the Ab Initio Study of the Electronic Properties of Crystals. *Zeit. Kristallogr.* **2005**, *220*, 571–573.

(80) Dovesi, R.; Saunders, V. R.; Roetti, C.; Orlando, R.; Zicovich-Wilson, C. M.; Pascale, F.; Doll, K.; Harrison, N. M.; Civalleri,; Bush, I. J. et al. CRYSTAL09 User's Manual. 2010.

(81) Perdew, J. P.; Ruzsinszky, A.; Csonka, G. I.; Vydrov, O. A.; Scuseria, G. E.; Constantin, L. A.; Zhou, X.; Burke, K. Restoring the Density-gradient Expansion for Exchange in Solids and Surfaces. *Phys. Rev. Lett.* **2008**, *100*, 136406.

(82) Grimme, S. Semiempirical GGA-type Density Functional Constructed with a Long-Range Dispersion Correction. *J. Comput. Chem.* **2006**, *27*, 1787–1799.

(83) Dunning, T. H. Gaussian Basis Sets for Use in Correlated Molecular Calculations. I. The Atoms Boron Through Neon and Hydrogen. *J. Chem. Phys.* **1989**, *90*, 1007–1023.

(84) Peterson, K.; Shepler, B.; Figgen, D.; Stoll, H. On The Spectroscopic and Thermochemical Properties of ClO, BrO, IO, and their Anions. *J. Phys. Chem. A* **2006**, *110*, 13877–13883.

(85) Metz, B.; Stoll, H.; Dolg, M. Small-core Multiconfiguration-Dirac-Hartree-Fock-adjusted Pseudopotentials for Post-d Main Group Elements: Application to PbH and PbO. *J. Chem. Phys.* **2000**, *113*, 2563–2569.

(86) Frisch, M. J.; Trucks, G. W.; Schlegel, H. B.; Scuseria, G. E.; Robb, M. A.; Cheeseman, J. R.; Scalmani, G.; Barone, V.; Mennucci, B.; Petersson, G. A. et al. Gaussian 09 revision a.1. Gaussian Inc. Wallingford CT, 2009.

(87) Kendall, R. A.; Dunning, T. H.; Harrison, R. J. Electron Affinities of the First Row Atoms Revisited. Systematic Basis Sets and Wave Functions. *J. Chem. Phys.* **1992**, *96*, 6796–6806.

(88) Tanaka, K.; Takahashi, T.; Ban, T.; Kondo, T.; Uchida, K.; Miura, N. Comparative Study on the Excitons in Lead-halide-based Perovskite-type Crystals $CH_3NH_3PbBr_3CH_3NH_3PbI_3$. *Solid State Communications* **2003**, *127*, 619–623.

(89) Chiarella, F.; Zappettini, A.; Licci, F.; Borriello, I.; Cantele, G.; Ninno, D.; Cassinese, A.; Vaglio, R. Combined Experimental and Theoretical Investigation of Opti-

cal, Structural, and Electronic Properties of CH3NH3SnX3 Thin Films (X=Cl,Br). *Phys. Rev. B Condens. Matter Mater. Phys.* **2008**, *77*, 045129.

(90) Howie, R.; Moser, W.; Trevena, I. The Crystal Structure of Tin(II) Iodide. *Acta Cryst.* **1972**, *B28*, 2965–2971.

(91) Hatch, D.; Stokes, H. Classification of Octahedral Tilting Phases in the Perovskite-like A_2BX_4 Structure. *Phys. Rev. B* **1987**, *35*, 8509–8516.

(92) Hatch, D.; Stokes, H.; Aleksandrov, K.; Misyul, S. Phase Transitions in the Perovskitelike A2BX4 Structure. *Phys. Rev. B* **1989**, *39*, 9282–9288.

(93) Mitzi, D. B. In *Progress in Inorganic Chemistry: vol. 48*; Karlin, K. D., Ed.; Wiley, 1999; pp 1–122.

(94) Lemmerer, A.; Billing, D. Lead Halide Inorganic-organic Hybrids Incorporating Diammonium Cations. *CrystEngComm* **2012**, *14*, 1954–1966.

(95) Papavassiliou, G.; Koutselas, I.; Terzis, A.; Whangbo, M.-H. Structural and Electronic Properties of the Natural Quantum-well System $(C_6H_5CH_2CH_2NH_3)_2SnI_4$. *Solid State Commun.* **1994**, *91*, 695–698.

(96) Li, Y.; Lin, C.; Zheng, G.; Cheng, Z.; You, H.; Wang, W.; Lin, J. Novel $<$ 110 $>$-oriented Organic-inorganic Perovskite Compound Stabilized By N-(3-aminopropyl)imidazole with Improved Optical Properties. *Chem. Mater.* **2006**, *18*, 3463–3469.

(97) Chung, I.; Song, J.-H.; Im, J.; Androulakis, J.; Malliakas, C.; Li, H.; Freeman, A.; Kenney, J.; Kanatzidis, M. $CsSnI_3$: Semiconductor or Metal? High Electrical Conductivity and Strong Near-infrared Photoluminescence from a Single Material. High Hole Mobility and Phase-transitions. *J. Am. Chem. Soc.* **2012**, *134*, 8579–8587.

(98) Jin, H.; Im, J.; Freeman, A. Topological Insulator Phase in Halide Perovskite Structures. *Phys. Rev. B Condens. Matter Mater. Phys.* **2012**, *86*, 121102.

(99) Knutson, J.; Martin, J.; Mitzi, D. Tuning the Band Gap in Hybrid Tin Iodide Perovskite Semiconductors Using Structural Templating. *Inorg. Chem.* **2005**, *44*, 4699–4705.

(100) Borriello, I.; Cantele, G.; Ninno, D. Ab Initio Investigation of Hybrid Organic-inorganic Perovskites Based on Tin Halides. *Phys. Rev. B Condens. Matter Mater. Phys.* **2008**, *77*, 235214.

(101) Filip, M.; Eperon, G.; Snaith, H.; Giustino, F. Steric Engineering of Metal-halide Perovskites with Tunable Optical Band Gaps. *Nat. Commun.* **2014**, *5*, 5757.

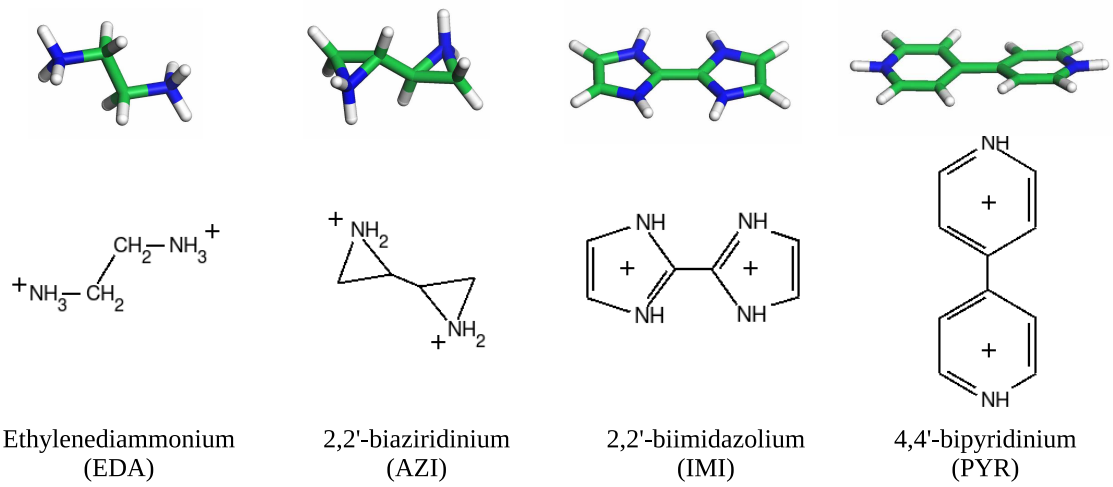

Ethylenediammonium (EDA) | 2,2'-biaziridinium (AZI) | 2,2'-biimidazolium (IMI) | 4,4'-bipyridinium (PYR)

Figure 1: Divalent organic cations intercalated in the hybrid perovskites.

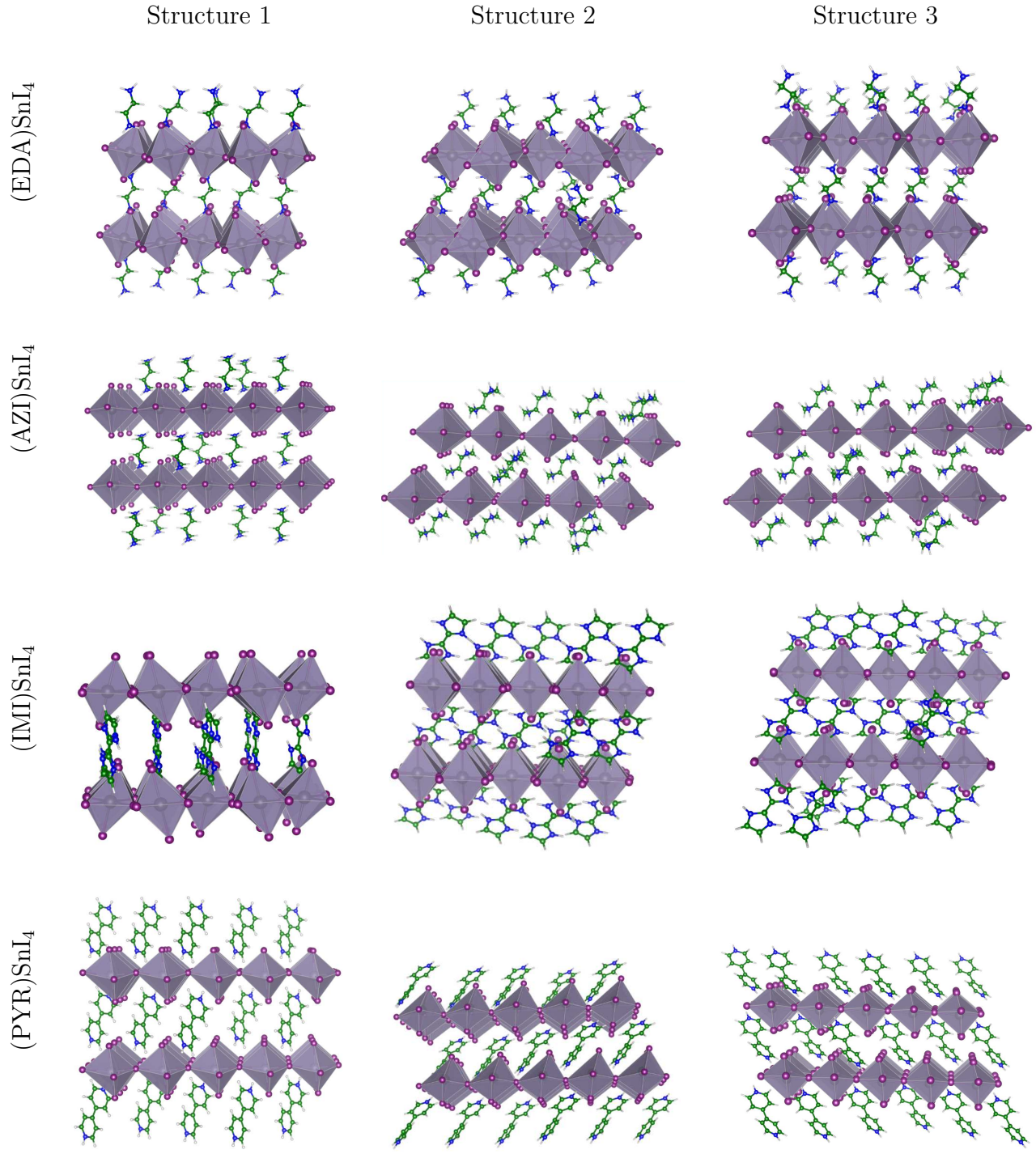

Figure 2: Optimized structures viewed along [100] direction.

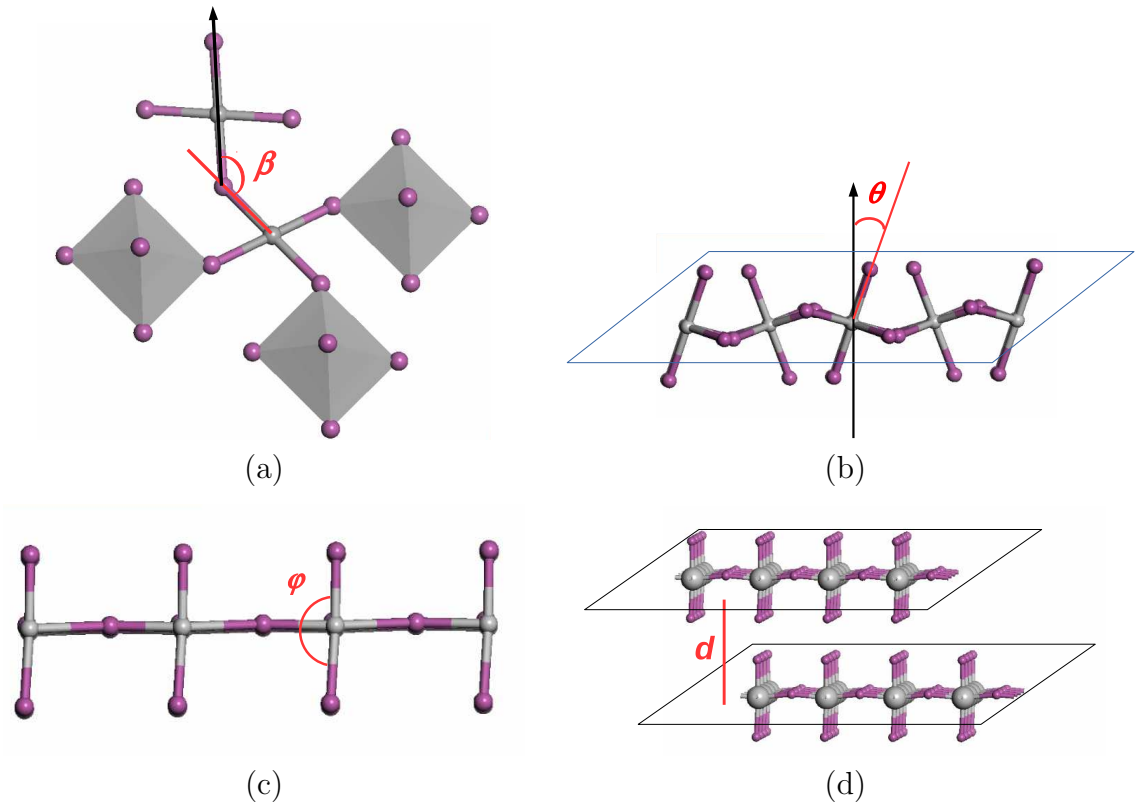

(a) (b) (c) (d)

Figure 3: Structural parameters for inorganic layers: (a) metal atom displacement angle, β; (b) octahedron tilting angle, θ; (c) octahedron deformation angle, ϕ; (d) interlayer distance, d.

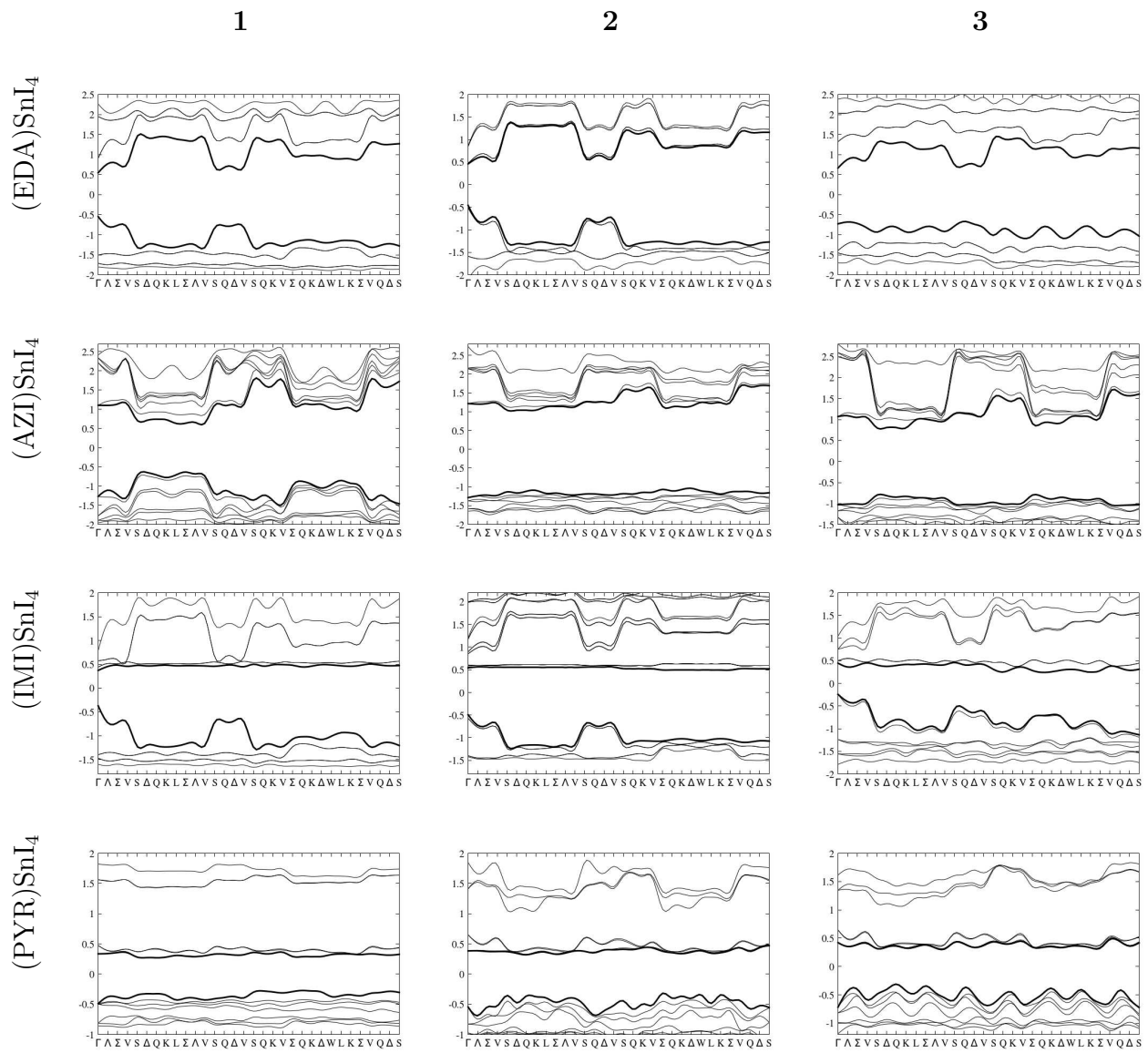

Figure 4: Electronic energy band profiles at the FR-DFT level.

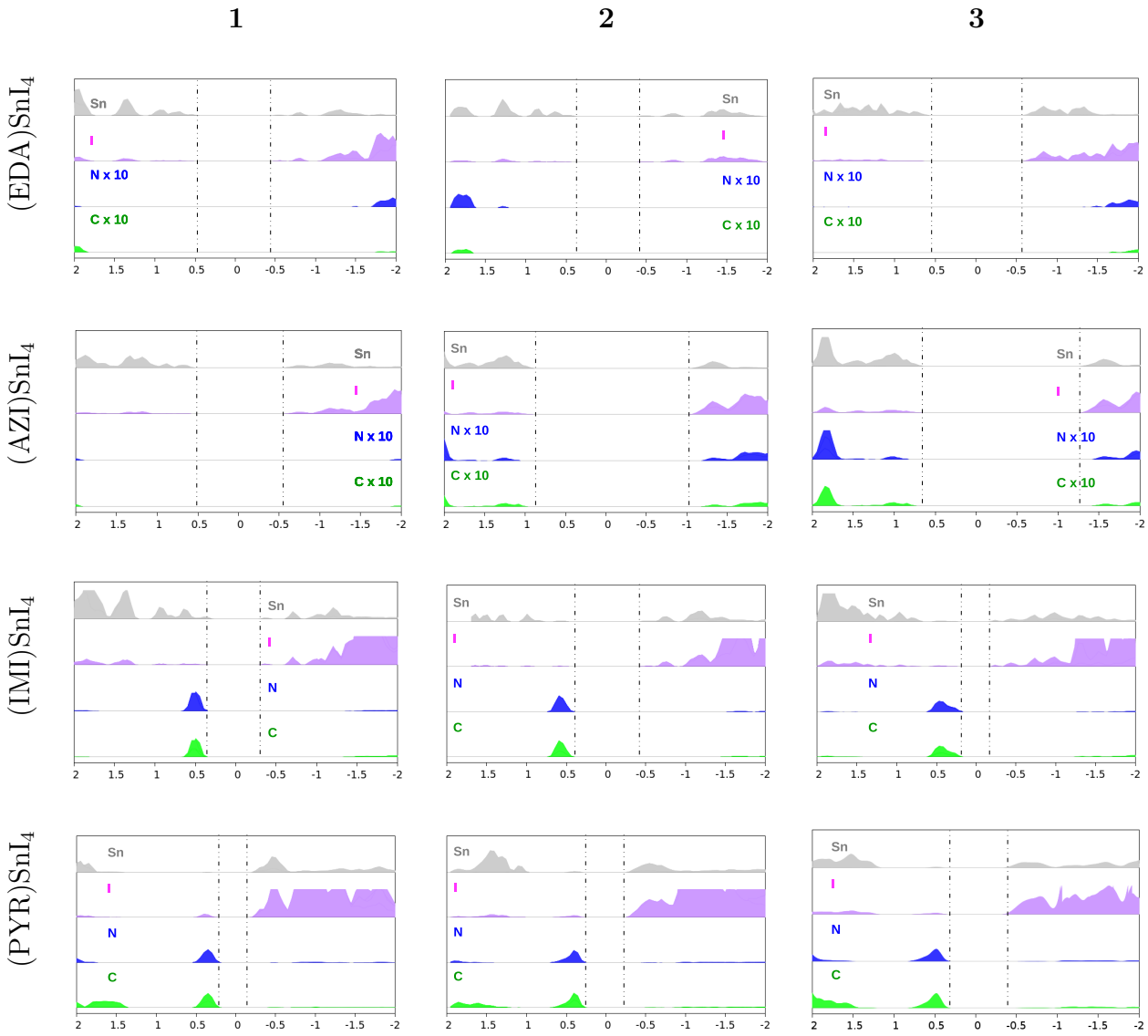

Figure 5: Projected density of states around the Fermi level at the FR-DFT level.

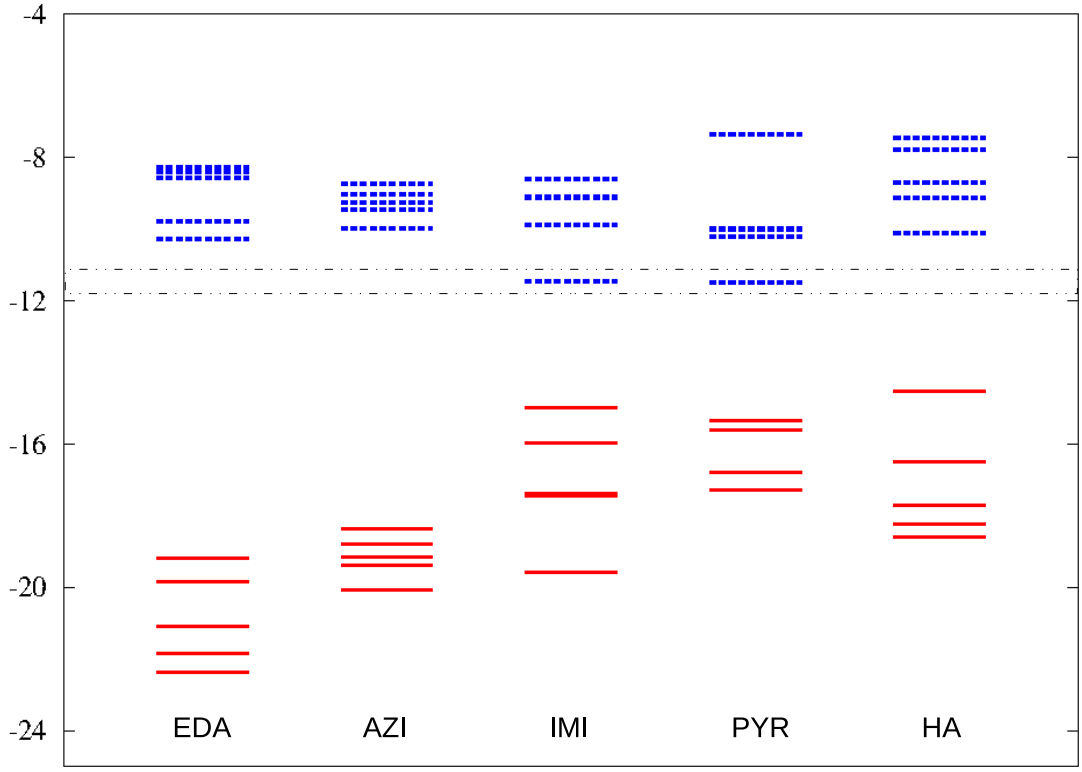

Figure 6: Energy (eV) of the highest occupied (red) and lowest unoccupied (blue) orbitals of the cations used in this work, along with histammonium (HA) cation.

Table 1: Cell parameters (Å and degrees), unit cell density (g/cm^3) and formation energies from eq. 2 (eV) for the optimized structures.

	a	b	c	α	β	γ	ρ_{cell}	E_{form}
Structure 1								
(EDA)SnI_4	8.85	8.93	10.27	85.4	76.6	89.3	2.91	-17.33
(AZI)SnI_4	6.21	6.09	10.14	89.0	103.1	87.9	3.17	-17.37
(IMI)SnI_4	8.73	8.92	10.19	90.3	81.6	90.0	3.23	-16.85
(PYR)SnI_4	6.31	6.50	11.42	88.3	97.1	110.6	3.00	-16.10
Structure 2								
(EDA)SnI_4	7.19	9.44	9.16	75.7	99.0	87.4	3.75	-18.02
(AZI)SnI_4	6.77	6.61	8.96	97.4	71.3	106.4	3.26	-17.62
(IMI)SnI_4	8.90	8.51	10.20	88.8	68.1	90.4	3.53	-17.44
(PYR)SnI_4	6.31	6.41	10.32	107.3	70.8	95.4	3.46	-16.62
Structure 3								
(EDA)SnI_4	8.17	8.28	9.18	81.0	97.5	89.7	3.76	-18.23
(AZI)SnI_4	6.68	6.57	8.65	85.3	110.9	103.3	3.43	-17.66
(IMI)SnI_4	8.20	9.24	9.49	81.4	108.9	87.9	3.79	-17.97
(PYR)SnI_4	6.47	6.26	10.16	107.4	103.5	95.3	3.47	-16.66

Table 2: Main structural parameters (degrees and Å) for inorganic layers: intra-layer metal displacement (β, Figure 3-a), octahedra tilting (θ, Figure 3-b), octahedra deformation (ϕ, Figure 3-c), equatorial (l_{eq}) and polar (l_p) $Sn-I$ bond lengths, and interlayer distance (d,Figure 3-d)

	Group	$(180^\circ - \beta)$	θ	$(180^\circ - \phi)$	l_{eq}	l_p	d
Structure 1							
(EDA)SnI_4	$P\bar{1}$	23.7/26.9	32.5	0.0	3.20/3.23	3.19	9.96
(AZI)SnI_4	$P1$	11.8/14.1	32.8	4.9	3.01/3.24	3.07/3.27	9.88
(IMI)SnI_4	$P\bar{1}$	1.9/10.8	33.0	0.0	3.11/3.14	3.23	10.08
(PYR)SnI_4	$P1$	25.3/25.7	31.3	6.7	2.92/3.71	3.13/3.16	11.33
Structure 2							
(EDA)SnI_4	$P\bar{1}$	18.5/25.9	32.7	0.0	3.12/3.19	3.02	8.98
(AZI)SnI_4	$P1$	18.6/23.1	30.5	4.6	2.91/3.77	3.14/3.21	8.48
(IMI)SnI_4	$P\bar{1}$	0.0/11.1	31.5	6.0	3.03/3.13	2.96/3.03	9.46
(PYR)SnI_4	$P1$	10.6/26.3	31.2	10.9	2.95/3.52	3.05/3.12	9.35
Structure 3							
(EDA)SnI_4	$P\bar{1}$	19.1/19.3	32.6	0.0	3.07/3.10	2.98	8.98
(AZI)SnI_4	$P1$	4.2/10.5	30.0	9.13	2.96/3.71	3.07/3.08	8.08
(IMI)SnI_4	$P1$	5.9/7.8	31.8	6.61	3.00/3.30	3.09/3.10	8.85
(PYR)SnI_4	$P1$	10.3/17.0	32.9	11.86	2.95/3.41	3.06/3.13	9.33

Table 3: Electronic band gaps (eV) computed for dicationic tin iodide perovskites with scalar (SR) and full relativistic (FR) pseudopotentials, at the DFT and GW level.

	E_g^{SR}	E_g^{FR}	SOC correct. (a)	$E_g^{GW}(\Gamma)$	$E_g^{SR}(\Gamma)$	GW correct. (b)	E_g (c)
Structure 1							
(EDA)SnI_4	1.33	1.10	-0.23	2.47	1.33	1.14	**2.24**
(AZI)SnI_4	1.53	1.27	-0.26	4.19	2.51	1.69	**2.96**
(IMI)SnI_4	0.96	0.74	-0.22	2.05	0.96	1.10	**1.84**
(PYR)SnI_4	0.79	0.54	-0.25	2.23	0.99	1.24	**1.78**
Structure 2							
(EDA)SnI_4	1.14	0.92	-0.22	2.35	1.14	1.21	**2.13**
(AZI)SnI_4	2.37	2.08	-0.29	3.41	2.67	0.74	**2.82**
(IMI)SnI_4	1.19	0.95	-0.24	1.81	1.20	0.62	**1.57**
(PYR)SnI_4	0.86	0.64	-0.22	2.18	1.09	1.09	**1.73**
Structure 3							
(EDA)SnI_4	1.49	1.33	-0.16	2.32	1.57	0.75	**2.08**
(AZI)SnI_4	1.87	1.60	-0.27	3.41	2.23	1.18	**2.78**
(IMI)SnI_4	0.62	0.49	-0.13	1.47	0.62	0.85	**1.34**
(PYR)SnI_4	0.84	0.62	-0.22	2.40	1.31	1.09	**1.71**

(a) Difference between columns 3 and 2: $E_g^{FR} - E_g^{SR}$.
(b) Difference between columns 5 and 6: $E_g^{GW}(\Gamma) - E_g^{SR}(\Gamma)$.
(c) Best estimate of the band gap from eq. 1, or equivalently E_g^{FR} + GW correction (column 3 + 7).

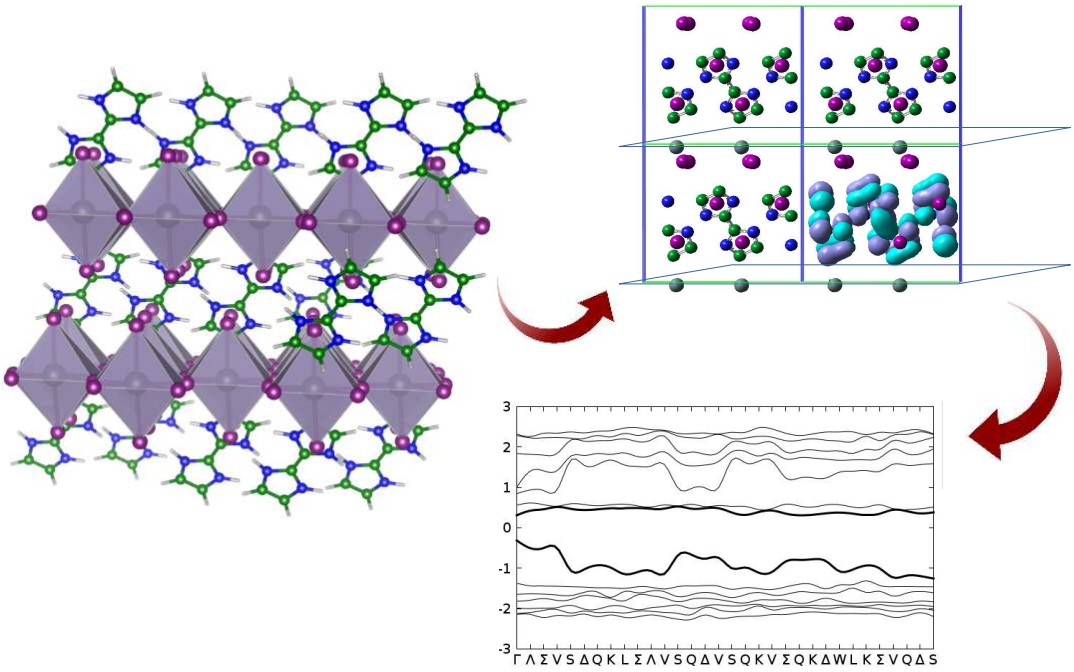

For Table of Contents Only.